Surface Science 618 (2013) 53–61

Contents lists available at ScienceDirect

Surface Science

journal homepage: www.elsevier.com/locate/susc

# Quantification of electronic band gap and surface states on $FeS_2$(100)

F.W. Herbert [a,b], A. Krishnamoorthy [a,b], K.J. Van Vliet [a], B. Yildiz [b,c,*]

[a] Department of Materials Science and Engineering, Massachusetts Institute of Technology, Cambridge, MA 02139, USA
[b] Laboratory for Electrochemical Interfaces, Massachusetts Institute of Technology, Cambridge, MA 02139, USA
[c] Department of Nuclear Science and Engineering, Massachusetts Institute of Technology, Cambridge, MA 02139, USA

ARTICLE INFO

*Article history:*
Received 11 June 2013
Accepted 20 August 2013
Available online 28 August 2013

*Keywords:*
Scanning tunneling spectroscopy
Surface states
Density functional theory

ABSTRACT

The interfacial electronic properties and charge transfer characteristics of pyrite, $FeS_2$, are greatly influenced by the presence of electronic states at the crystal free surface. We investigate the surface electronic structure of $FeS_2$ (100) using scanning tunneling spectroscopy (STS) and interpret the results using tunneling current simulations informed by density functional theory. Intrinsic, dangling bond surface states located at the band edges reduce the fundamental band gap $E_g$ from 0.95 eV in bulk $FeS_2$ to 0.4 ± 0.1 eV at the surface. Extrinsic surface states from sulfur and iron defects contribute to Fermi level pinning but, due to their relatively low density of states, no detectable tunneling current was measured at energies within the intrinsic surface $E_g$. These findings help elucidate the nature of energy alignment for electron transfer processes at pyrite surfaces, which are relevant to evaluation of electrochemical processes including corrosion and solar energy conversion.



## 1. Introduction

Pyrite or $FeS_2$ is a semiconducting mineral for which the electronic structure has been intensively studied in relation to reactivity in geochemical [1–4] and bio-catalytic [5–7] processes, as well as for photovoltaic (PV) and photoelectrochemical properties [8–12]. Heterostructures of $FeS_2$ and perovskite oxides such as $LaAlO_3$ have recently been proposed as promising devices for spintronics applications [13]. $FeS_2$ is also known to form in anoxic, $H_2S$-containing environments such as those encountered by the oil and gas industry, where it is typically incorporated into passive corrosion films on steel structures [14]. In the following, we review the literature and discuss the surface electronic structure of pyrite and its characterization by scanning tunneling microscopy and density functional theory calculations.

### 1.1. Surface electronic structure of pyrite

Despite this wide ranging scientific interest in pyrite, important questions remain regarding the fundamental electronic properties of its free surface, which is critical towards understanding how energy levels align during interfacial charge exchange with reduction–oxidation (redox) species in the surrounding environment. For example, the reactivity of semiconducting materials can be significantly altered by surface states that are either intrinsic to the crystal termination or have arisen from the presence of crystalline defects at the surface, such as steps, kinks, dislocations, impurities or vacancies [15,16]. Moreover, in the context of PV, low open circuit voltages (VOC) of <200 mV (or ~21% of the widely accepted bulk band gap of 0.95 eV) have been attributed to poor interfacial electronic properties of synthetic $FeS_2$ systems [12]. We have recently reported density functional theory (DFT) calculations on the electronic structure of pristine and defective $FeS_2$(100) surfaces [17]. The aim of the present article is to combine rigorous first-principles calculations with experimental results obtained using scanning tunneling spectroscopy (STS) to provide a complete description of how interfacial electronic states affect the band gap and electronic properties of the pyrite surface. The crystal structure of $FeS_2$ (space group $Pa3$) comprises two interpenetrating cation ($Fe^{2+}$) and anion ($S_2^{2-}$) face centered cubic (fcc) sublattices, the latter of which is made up of $S_2$ persulfide dimers aligned along the cube diagonal direction <111>. Pyrite is a compound, *d*-band semiconductor with an electronic structure that can be qualitatively understood with the aid of a simple ligand field model [18]. Each $Fe^{2+}$ ion in the bulk is octahedrally coordinated by $S_2^{2-}$ ions (symmetry group $O_h$), creating a strong ligand field that splits the metal *d* states into non-bonding, triply degenerate Fe 3*d* $t_{2g}$ states ($d_{xy}$, $d_{yz}$ and $d_{x^2-y^2}$) at the top of the valence band (VB). The conduction band (CB) minimum consists of doubly degenerate Fe 3*d* $e_g$ states ($d_{z^2}$ and $d_{x^2-y^2}$) hybridized with S $pp\sigma^*$ orbitals. An indirect band gap $E_g$ of 0.83–1.01 eV has been measured in synthetic, bulk $FeS_2$ using various optical [19,20], photoconductivity [21,22] and X-ray absorption/emission spectroscopy studies [23]. At the unreconstructed (100) surface termination of pyrite, the predominant growth and cleavage face, the symmetry of the $Fe^{2+}$ site is reduced from $O_h$ to square pyramidal $C_{4v}$, leading to a loss of degeneracy among the Fe 3*d* $t_{2g}$ and $E_g$ states. These further split into two discrete, intrinsic surface states associated with the Fe dangling bond. Recent density functional theory (DFT) calculations are consistent in identifying these two pronounced

* Corresponding author at: Department of Nuclear Science and Engineering, Massachusetts Institute of Technology, Cambridge, MA 02139, USA.
*E-mail address:* byildiz@mit.edu (B. Yildiz).

0039-6028/$ – see front matter © 2013 Elsevier B.V. All rights reserved.
http://dx.doi.org/10.1016/j.susc.2013.08.014

surface states to be located around the VB maximum (Fe-$d_{x^2}$ character) and at the CB minimum (Fe-$d_{x^2-y^2}$). The magnitude of the surface states decays almost entirely to zero beyond approximately three atomic layers into the bulk [24]. As a result it is theoretically estimated that $E_g$ at the $FeS_2$ free surface is reduced by up to 0.3–0.4 eV, as compared to the bulk value (Table 1). In addition to the intrinsic surface states on $FeS_2$(100), computational studies have identified a series of further surface states that appear within the fundamental surface $E_g$ local to interfacial point defects [7,17,24]. We refer to such states as "defect" or "extrinsic" states to differentiate them from intrinsic surface states. Significant concentrations of neutral sulfur monomer vacancies $V_S$ have been measured by X-ray photoelectron spectroscopy (XPS) on fractured $FeS_2$(100) [25–28] as well as in situ ion-bombarded [29] and annealed [30] growth faces. Indeed, the formation energy $\Delta H_f$ for $V_S$ is estimated to be as low as 0.1 eV experimentally [30] and 0.4–0.42 eV computationally [24,31], suggesting that up to 20% of surface sulfur sites on $FeS_2$(100) may be vacant at ambient temperatures of 298 K, and therefore $V_S$ electronic states are prevalent. Moreover, neutral Fe vacancies $V_{Fe}$ on the surface have been imaged at the atomic scale by scanning tunneling microscopy (STM) and shown to comprise a comparably high fraction of the surface [32]. Via DFT, Zhang et al. predicted a maximum surface $E_g$ of 0.72 eV for stoichiometric (Fe:S = 1/2) $FeS_2$(100), but only 0.56–0.71 eV and 0–0.3 eV for sulfur-deficient and sulfur-rich surfaces, respectively. Other authors have theoretically calculated that $V_S$ at the surface can reduce the surface $E_g$ by more than this, even making the surface metallic [24]. Such arguments have been used, for example, to explain the low resistivity ($O(10^{-1})$ Ω·cm) of manufactured pyrite thin films for PV applications [33]. Despite this recognition that $FeS_2$(100) interfaces are non-stoichiometric, there remains a need to demonstrate experimentally the effect of defects on the electronic structure.

In this work, we define *surface* $E_g$ as the energy difference between the extrema of the intrinsic surface bands that extend into the band gap of the bulk material. Discrete defect states lying within the fundamental $E_g$ are therefore not included in the quantification of surface $E_g$.

### 1.2. Quantitative analysis from scanning tunneling spectroscopy

The STM operating in ultra high vacuum (UHV) provides a controllable metal-vacuum-semiconductor tunnel junction to probe these electronic states at the surface. A limited number of STS studies on natural [34,35] and synthetic [36,37] $FeS_2$ single crystals have produced inconsistent results, with apparent band gaps ranging from ~0 eV to the accepted bulk value of 0.95 eV (Table 2), and a lack of detailed insight into the nature of the pyrite surface states. Here our aim is to determine the role of surface states in determining the surface $E_g$ through quantitative analysis of tunneling spectroscopy (STS) measurements. We adopt the approaches developed in modeling STS data from semiconductor surfaces that was advanced from the late 1980s by R.M. Feenstra and others. Early work began with the traditional cubic tetrahedrally bonded [38] and III–V [39] semiconductors, on which band edges and surface-related features could be determined to within an accuracy of ±0.03 eV. The concurrent development of tunneling spectrum models based on computations of potential distributions and tunneling current has helped identify the role of other physical phenomena in experimental STS spectra, such as tip-induced band bending (TIBB) [40] and surface states [41]. TIBB greatly affects the STS measurement of unpinned semiconductor surfaces, in which changes in the tip-induced electric field lead to an unrestricted accumulation or depletion of charge carriers at the surface which act to screen the tip potential. In this case, the electron chemical potential $\mu_e$ in the sample shifts freely with applied bias, distorting the CB and VB near the surface. However, if surface states are present on the sample, charges from the bulk bands can fall into them and $E_F$ becomes pinned at the level to which the surface states are occupied. STS spectra of $E_F$-pinned surfaces typically yield more consistent band onsets and are less affected by localized quantum effects such as inversion or accumulation currents arising from TIBB. These phenomena are discussed in more detail in Section 3.1, in the context of our experimental results.

**Table 1**
Calculated bulk band gap $E_g$, and surface $E_g$, both for pristine and defective $FeS_2$(100). Defective surface here refers to the presence of a single sulfur vacancy $V_S$ in a single 1 × 1 unit surface supercell.

| Bulk $E_g$(eV) | Pristine surface $E_g$(eV) | Defective surface $E_g$(eV) | Ref. |
|---|---|---|---|
| 0.87 | 0.40 | 0.27 | [7] |
| 1.02 | 0.56–0.71 | N/A | [31] |
| 0.86 | 0.55 | 0–0.2 | [17] |
| 0.90 | 0.60 | 0.0 | [24] |

**Table 2**
Experimental surface Eg measurements by scanning tunneling spectroscopy (STS).

| Sample/surface type | Surface $E_g$ measurement (eV) | Ref. |
|---|---|---|
| Natural, fractured in UHV | 0.04 | [34] |
| Natural, fractured in air | 0.20 | [35] |
| Synthetic, as-grown surface | 0.95 | [36] |
| Synthetic, fractured in air | 0.00 | [37] |

### 1.3. First-principles modeling of surface states

In this paper, we report systematic STS measurements obtained on high-purity $FeS_2$(100) single crystals. In parallel, DFT-computed DOS was used to theoretically predict the existence of both intrinsic and defect-related surface states on this material. Using the DOS derived from DFT, we modeled the effect of intrinsic surface states on $FeS_2$ tunneling spectra, and compared the model results to our experimental data. When the intrinsic surface states were considered to be surface-localized acceptor/donor states that pin the Fermi level, as has been suggested by Rosso [4], we found that no realistic range of input parameters was able to replicate the experimental spectra. However, a reasonable fit was obtained when it was assumed that the intrinsic surface states overlap continuously with the $FeS_2$ bulk CB and VB, and therefore contribute to tunneling within the fundamental bulk $E_g$ without pinning $E_F$. From this modeling-enabled interpretation of our experimental measurements, we estimate the effective surface $E_g$ to be 0.4 ± 0.1 eV. Further, our modeling suggests that neutral surface point defects $V_S$ and $V_{Fe}$ can contribute extrinsic surface states that appear discretely within $E_g$, additionally pinning the surface Fermi level due to charge redistribution over significant fractions of the surface. We do not observe any detectable tunneling current from these extrinsic states due to their low areal and state density, coupled with a low perpendicular tunneling probability. These results demonstrate the effectiveness of applying first-principle calculations to infer meaningful data from experimental tunneling spectra — especially those in which clear features cannot be distinguished in the raw tunneling current-bias response. In doing so, we reconcile the theoretical surface electronic structure of $FeS_2$(100) with the computational and theoretical calculations performed by the present authors as well as others, with implications toward understanding interfacial charge transfer in both natural and synthetic pyrite-based systems. As well as being informative for surface reactivity, the results may help explain the low open circuit voltage of synthetic $FeS_2$ PV devices, which could be related to a reduced surface $E_g$ and Shockley–Read–Hall recombination at mid-gap defect states.

## 2. Methods

### 2.1. Experimental

High purity single crystals of $FeS_2$ were synthesized by chemical vapor transport (CVT) in closed quartz ampoules, based on techniques

described in Refs. [20,42]. Raw materials were procured from Alfa Aesar (Haverhill, MA). A 1:2 stoichiometric mixture of 99.999% pure Fe powder and 99.995% S granules totaling 4 g – along with ~0.3 g of 98% pure anhydrous $FeBr_3$ – was sealed in an evacuated, 20 cm long quartz tube and heated to 700 °C for 15 days to form polycrystalline pyrite aggregates. This precursor pyrite was removed, cleaned in acetone and methanol and resealed in a similar quartz tube with 0.3 g of fresh $FeBr_3$ and a small amount of solid sulfur to provide a sulfur-rich environment for single crystal growth. The quartz tube was placed in a temperature gradient from 700 to 550 °C, with the polycrystalline pyrite charge placed at the hot end, and left for up to 30 days. The mechanism of pyrite growth by CVT is described in Ref. [12]. The resulting crystals were typically cuboidal in shape with 5–10 mm edge lengths and predominant {100} growth faces as determined by electron backscatter diffraction (EBSD) and single crystal X-ray diffraction (XRD). As-grown crystals were checked for phase purity using Raman spectroscopy and were found to be n-type semiconducting, with a donor concentration $N_D$ in the range 1–5 × $10^{16}$ $cm^{-3}$ by Hall measurement at 21 °C. In addition, an indirect $E_g$ of 0.9–0.95 eV was detected by optical absorption on $FeS_2$ single crystals polished down into 200 μm-thick plates. A full description and characterization of the pyrite samples can be found in the Supporting Information. Scanning tunneling microscopy (STM) was carried out using a VT-AFM system (Omicron Nanotechnology, GmbH, Germany) under UHV at pressures in the $10^{-10}$ Torr range. We used electrochemically etched Pt–Ir tips that were annealed at 150 °C for 2 h under UHV to remove absorbed $H_2O$ and hydrocarbons prior to taking measurements. Single crystal, {100} growth faces of $FeS_2$ were investigated by STM subsequent to ex situ cleaning by the following procedure: sealed quartz tubes containing freshly-grown crystals were opened in a glove box under a high purity, 95% $N_2$–5% $H_2$ environment to control surface oxidation and were ultrasonically cleaned in acetone and methanol to remove residual $Br_2$, which was proposed to be a source of contamination in previous STM studies of synthetic pyrite [37]. Samples were clamped in a custom made aluminum stage and transferred to vacuum within <1 min to minimize exposure to laboratory air. STM and STS results from samples prepared in this way were compared with similar data obtained using in situ fractured, synthetic $FeS_2$ single crystals which are known to have stepped, (100)-oriented faces [43,44]. The STS results from as-grown and in situ fractured surfaces were quantitatively indistinguishable. X-ray photoelectron spectroscopy-valence band (XPS-VB) spectra were obtained at the U12A beam line of the National Synchrotron Light Source (Brookhaven National Laboratory, Upton, NY), using a photon excitation energy of 210 eV. Single crystal growth faces of $FeS_2$ were prepared in a similar fashion as described above and were cooled in situ under UHV to approximately −170 °C before performing XPS-VB measurements.

### 2.2. Computational

Full details on the density functional theory computational methods on the $FeS_2$ system can be found in Ref. [17]. Briefly, DFT calculations were performed using the projector-augmented wave method with the Vienna ab initio simulation package (VASP). We employed the Perdew–Burke–Ernzerhof (PBE) form of the general gradient approximation (GGA). To accurately capture the delocalization of the electrons in transition metal compound, we use the DFT + U method of Dudarev et al. [45]. We use the previously parameterized value of $U - J = 1.6$ eV for calculations involving pyrite [17]. We employ a high plane-wave cutoff of 350 eV and all the calculations are run until energies are converged to within 5 × $10^{-5}$ eV in each self-consistency cycle and forces on all ions are converged to within 0.05 eV/Å. All crystal structures presented in this paper were generated using the VESTA visualization program [46]. Computations of tunneling current for simulating STS data were carried out using the full three-dimensional (MultInt3) version of the open-source program SEMITIP v.6, courtesy of R.M. Feenstra [47]. The program is a Poisson solver that treats the case of a hyperbolic-shaped tip in tunneling contact with a semiconductor sample. A complete description of the physics involved in the calculations is given in Refs. [41,40,48–50]. Table 3 summarizes the key input parameters for tunneling current calculations that are related to the electronic properties of the tip and sample, and the geometry of the tunneling simulation. Given the large number of input variables, we found an efficient approach to modeling proceeded along the following routine: first, all known variables are assigned their experimentally or computationally measured values. Second, the tip-sample separation distance $s$ and tip radius $R$ were estimated based on previous literature [40,51]. Finally, we allocated to the remaining free variables a physically realistic range of values and performed a sensitivity analysis to optimize the fits (see Supp. Info.). In practice, it was found that only the major semiconductor properties such as donor concentration $N_D$, conduction band effective mass $m_c$ and heavy hole effective mass $m_{hh}$, along with the contact potential $\Delta\varphi$, had a significant quantitative influence on the model output of tunneling current.

**Table 3**
Input parameters for tunneling spectroscopy simulations using the SEMITIP program.

| Property | Symbol | Value used | Unit |
|---|---|---|---|
| Donor concentration[a] | $N_D$ | $1 \times 10^{16}$ | $cm^{-3}$ |
| CB effective mass[b] | $m_c$ | 0.09–0.15 $m_e$ | N/A |
| Heavy hole effective mass[b] | $m_{hh}$ | 0.6–2.0 $m_e$ | N/A |
| Contact potential[c] | $\Delta\varphi$ | 1.0–1.2 | eV |
| Tip-sample separation | $s$ | 0.8–1.0 | nm |
| Tip radius | $r$ | 50 | nm |

[a] Bulk Hall measurement on FeS2 single crystals in this work.
[b] Effective masses optimized from DFT-computed band structure.
[c] Contact potential estimated from DFT calculation of work function, supported by experimental evidence in Ref. [12].

In the tunneling spectrum model, we accounted for the existence of charge accumulating surface states on $FeS_2$ by introducing them explicitly into SEMITIP, either as a pair of Gaussian-distributed functions (Fig. 1a), or as a uniform band across a predefined energy range (Fig. 1b). For each of these surface state distributions, we fixed the charge neutrality level $E_N$. Here, $E_N$ connotes the energy level below which states are neutral when filled and positively charged when empty, or, conversely, above which they are negatively charged when filled and neutral when empty. In the case of the double Gaussian distribution, the additional variables of centroid energy (the displacements of the states in Energy either side of $E_N$) and the full width half maximum (FWHM) of the peaks were assigned optimized values for fitting (see Supp. Info.). It is important to note that surface states in the tunneling model are treated as completely localized at the surface, i.e., their magnitude does not decay exponentially into the bulk. Surface states thus affect only the electrostatic potential part of the calculation and are not included in the computation of tunneling current.

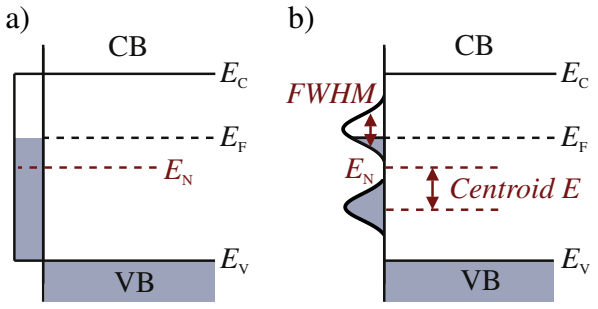


**Fig. 1.** Distributions of surface states as defined in the SEMITIP program: (a) uniform distribution, with charge neutrality level $E_N$ and (b) double Gaussian distribution, where FWHM is the full width half maximum of the peaks, and the centroid energy defines their separation either side of $E_N$. Filled states are shaded in gray. VB and CB refer to the bulk valence and conduction bands respectively.

## 3. Results and discussion

### 3.1. Current-separation and current–voltage tunneling spectroscopy

STS results were obtained experimentally on single crystal $FeS_2$(100), measured at various tip-sample separation distances $s$. Due to the well-known exponential dependence of tunneling current $i_{tunn}$ on $s$, the onset of detectable tunneling current either side of 0 V bias (nominally the VB and CB edges), which give rise to an apparent surface $E_g$ in the data, depends on the initial set point tunneling conditions for STS acquisition. Therefore we normalize the data to the constant tip-sample separation so at which a consistent "gap" of approximately 0.5 eV is visible. However, we explain why the quantification of $E_g$ directly from STS spectra in this manner can be misleading, since it does not account for the phenomenon of tip-induced band bending, in which the band structure of the sample is distorted by the local electric field from the tip. Understanding which electronic states contribute to tunneling and affect TIBB requires more detailed modeling of the tunneling spectra, described in full in the following Section 3.2. Stable STM images were initially taken at relatively low magnification ($500 \times 500$ nm$^2$) to locate sizeable flat terraces for consistent STS data acquisition (Fig. 2a). The tip was subsequently scanned over $20 \times 20$ nm$^2$, or smaller, atomically-flat areas (Fig. 2b) to obtain tunneling spectroscopic information at various set point currents ($i_{set}$) and biases ($V_{set}$). The tip was then briefly paused over randomly selected points during which the feedback loop was turned off for 1 ms to acquire current-separation $i(s)$ or current-bias $i(V)$ spectra.

The magnitude of the measured tunneling current $i_m$ as a function of bias voltage $V$ is affected by the vertical tip displacement at the instant of STS acquisition. This separation distance $s$ can be related to the set point conditions $i_{set}$ and $V_{set}$ through the simple exponential decay relation $i(s) = i_o \exp(-2\kappa s)$, where $i_o$ is a constant and $\kappa$ is the vacuum tunnel coefficient, otherwise known as the decay constant. $\kappa$ is approximated for one-dimensional tunneling and reasonable $V_{set}$ by [52,53]:

$$\kappa = \sqrt{\frac{2m_e}{\hbar}\left(B - \frac{|eV_{set}|}{2}\right) + |k_\parallel|^2} \quad (1)$$

where $m_e$ is the electron mass, $B$ is the effective tunneling barrier and $k_\parallel$ is the parallel wave vector of the tunneling electrons. The decay constant $\kappa$ for pyrite was determined via $i(s)$ spectroscopy at a range of different setpoint biases. Fig. 3a shows the $i(s)$ response at $V_{set} = -1.4$ V (main image) and $V_{set} = 0.4$, 1.2 and 2.0 V (inset), each averaged over approximately 20 measurements at different points on the $FeS_2$ sample surface. The magnitude of $\kappa$ over the range $-2\text{ V} \le V \le 2\text{ V}$ varied linearly from approximately 0.3 Å$^{-1}$ at large bias to 0.5 Å$^{-1}$ near 0 V, and was symmetric for negative and positive bias (Fig. 3b). The average effective tunneling barrier $B$, calculated using Eq. (1) and assuming $k_\parallel = 0$, was 3.2 eV. This corresponds to the average work function between the metallic tip and the pyrite sample at the tunnel junction. A comparable tunneling barrier height of 2.2 eV was previously measured on synthetically grown pyrite single crystals by Fan and Bard [36].

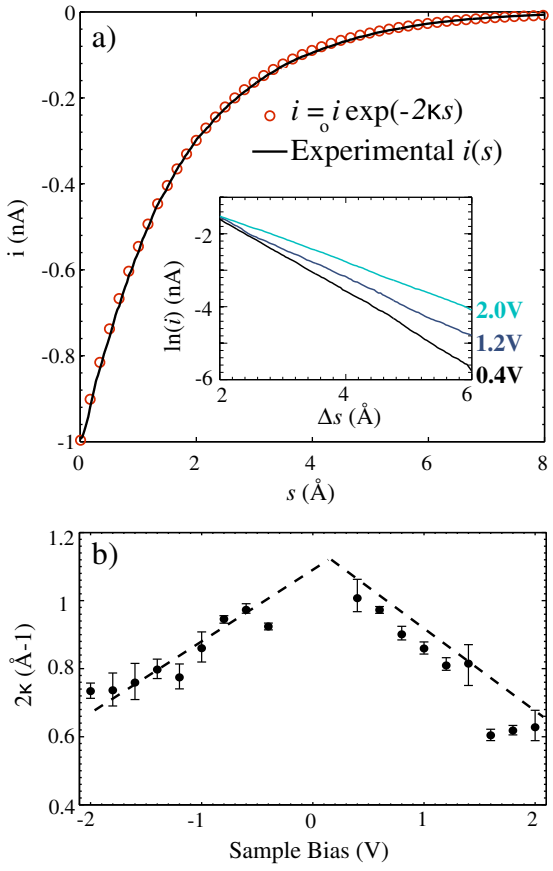


**Fig. 3.** (a) Tunneling current $i$ as a function of tip-sample separation s at a set point bias of −1.4 V (solid line). A fitted exponential function $i = i_o \exp(-2\kappa s)$ with decay constant $2\kappa = 0.80$ Å$^{-1}$ is overlaid on the experimental data (open circles). Inset: experimental data for 0.4, 1.2 and 2.0 V biases, plotted on a log scale. (b) $2\kappa$ variation across the bias range used in this work. The dashed lines are to guide the eye, and do not represent a fit to the data.

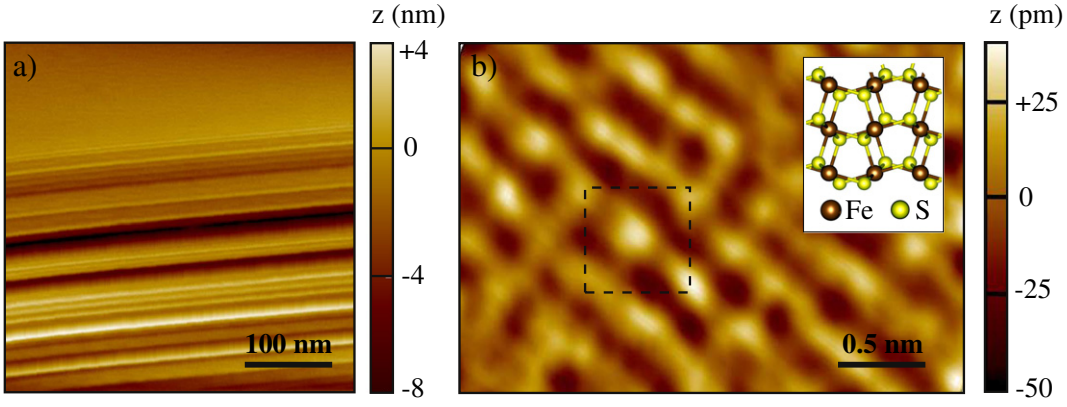


**Fig. 2.** (a) Scanning tunneling spectroscopy (STM) image of as-grown $FeS_2$(100) surface, showing large atomic terraces with step edges oriented along the <100> direction. Tunneling conditions: $V_{set} = -1.5$ V, $i_{set} = 0.5$ nA. Scanning tunneling spectroscopy (STS) was performed on selected $20 \times 20$ nm$^2$ flat areas, (b). Fe atoms are resolved on the $FeS_2$(100) surface. The inset figure displays an atomic model for comparison, with one unit cell of Fe atoms outlined by the dashed square. Tunneling conditions: $V_{set} = 0.2$ V, $i_{set} = 4$ nA.

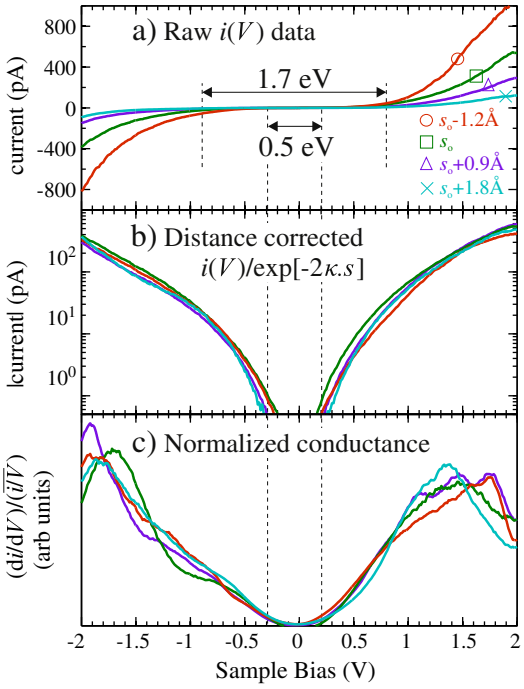


**Fig. 4.** (a) Tunneling current–voltage $i(V)$ curves measured on $FeS_2$(100) with varying tip-sample separations $s$. $s_o$ corresponds to a tunneling set point of $V_{set} = 1.5$ V and $i_{set} = 200$ pA. (b) The same $i$-$V$ data normalized to constant tip-sample separation, plotted on a logarithmic $i$ axis to facilitate comparison. (c) Normalized conductance $(di/dV)/\overline{(i/V)}$ as a measure of local density of states (DOS). An estimate of surface band gap $E_g$ width using the instrument resolution of 1 pA is ~0.5 eV.

Fig. 4a displays a series of individual $i(V)$ spectra taken at four different values of $s$, where the set point $V_{set} = 1.5$ V and $i_{set} = 200$ pA was arbitrarily chosen as the reference separation $s_o$. The other values of $s$ were calculated relative to $s_o$ using the exponential decay relation for tunneling with the experimentally-determined $\kappa$ from $i(s)$ spectroscopy. At more positive $s$ (larger tip-sample separation), the measured current around 0 V becomes very small and the $E_g$ appears larger, up to approximately 1.7 eV for $s = s_o + 1.8$ Å. To correct for the exponential decay in transmission coefficient for tunneling, the $i(V)$ data are normalized in Fig. 4b to a constant tip-sample separation by converting the measured current $i_m$ to "distance corrected current" $i_s = i_m \exp[2\kappa(V)s]$, where $s = 0$ at the reference separation distance $s_o$. Separation distance-normalized data are displayed with a logarithmic current scale to enable discrimination among spectra. The four curves overlap consistently, indicating that throughout the tunneling set point range used in this work the tunneling spectra give a true representation of the tunneling response without metallic behavior due to point contact at very small $s$, or anomalously insulating behavior at large $s$. Further, we normalize the data to normalized conductance $(di/dV)/\overline{(i/V)}$ (Fig. 4c) which is known to approximate the DOS in semiconducting or metallic samples [38]. We calculated $(di/dV)$ by numerical differentiation from the $i(V)$ response. To correct for the well-known divergence of the direct conductance $(i/V)$ at small values of $i$, $i/V$ was broadened to $\overline{i/V}$ using a Gaussian distribution described previously [39].

A first approximation of surface $E_g$ from the $i(V)$ response is 0.5 eV, obtained by taking the average voltage separation between the CB and VB current onsets at the lowest detectable current (Fig. 4b). Nevertheless, the direct quantification of surface $E_g$ in this manner does not account for the possible occurrence of TIBB. The large, localized electric field from the proximate tip extends through the vacuum region and into the surface of the pyrite sample. Consequently, a fraction of the applied potential can be dropped within the sample itself, causing the valence and conduction bands to bend and obscuring the energy scale of the measured STS spectra. A comprehensive description of TIBB can be found in previous reports [54,40,41,55], but the main points are outlined here for completeness. The contact potential $\Delta\varphi$ is defined as the difference in work function between the metal tip and the semiconductor:

$$\Delta\varphi = \varphi_m - \chi - (E_C - E_F) \quad (2)$$

where $\varphi_m$ is the metal work function, $\chi$ is the electron affinity of the semiconductor, and $E_C$ and $E_F$ are the conduction band minimum and Fermi level of the sample, respectively (Fig. 5a). Even in the absence of applied bias, a non-zero $\Delta\varphi$ leads to band bending and the formation of a depletion region in the sample. For example, a positive $\Delta\varphi$ produces upward band bending in the semiconductor as the Fermi level aligns with that of the tip; negative charge correspondingly accumulates at the surface to screen the potential (Fig. 5b). The effect is to shift the energy $E$ of any given state at the surface by an amount $\varphi_o$:

$$E - E_F = eV - \varphi_o. \quad (3)$$

When $E_F$ at the surface is unpinned in this manner, the resulting experimental $i(V)$ measurement can yield a very wide apparent surface $E_g$, as the band edges shift with the sweeping voltage and the onset of tunneling is delayed to more positive (for the CB) or negative (for VB) voltages (Fig. 5c). Such a situation arises on defect-free ZnO(110) surfaces [56], where the apparent band gap from STS can be larger than the accepted bulk gap of the material, or on GaN(1100) where quantitative $E_g$ determination was not possible [57]. Severe band bending can also introduce large tunneling currents from local states when the semiconductor $E_F$ is pushed into the VB (inversion) or CB (accumulation) [40,51]. The presence of intrinsic (dangling bond) surface states inside the fundamental $E_g$ on semiconductors typically limits TIBB by pinning $E_F$ (Fig. 5d) [41,53]. These states accumulate charge as they become

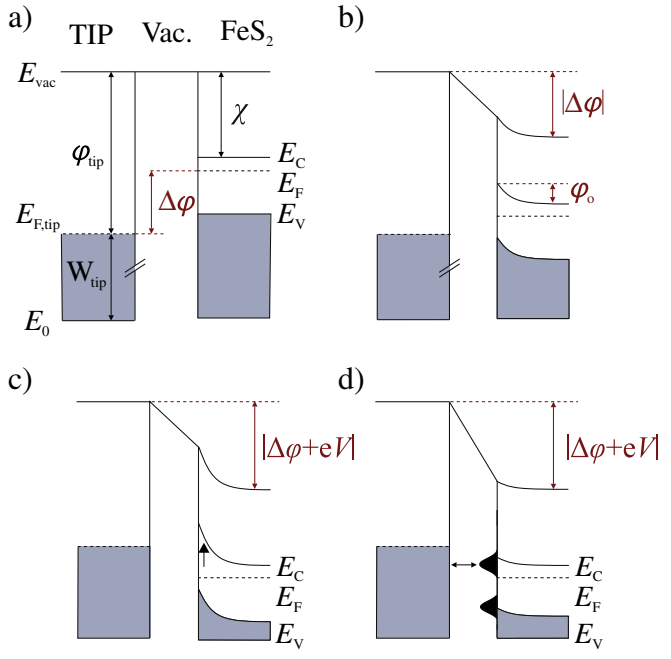


**Fig. 5.** Schematic energy band diagrams for an n-type pyrite sample where (a) tip and sample are not in tunneling contact; (b) there is an open circuit tunneling junction. With a positive contact potential $\Delta\varphi$, an upward band bending of magnitude $\varphi_o$ occurs. In addition to the parameters described in the text: $E_{vac}$ is the vacuum energy level, $E_o$ the ground level, and $E_V$ is the valence band maximum of the semiconductor. $W_{tip}$ is the energy difference between the metal's Fermi level and the bottom of the metal valence band, typically ~8 eV for PtIr tips. $E_{F,tip}$ is the tip Fermi level. All filled states are shaded in gray. (c) Upon applying a positive sample bias $V$, further upwards tip-induced band bending (TIBB) occurs if $E_F$ is unpinned. However, surface states, e.g. shaded in black in (d), can accommodate enough surface charge to pin $E_F$ and minimize TIBB (after Feenstra et al. [40]).

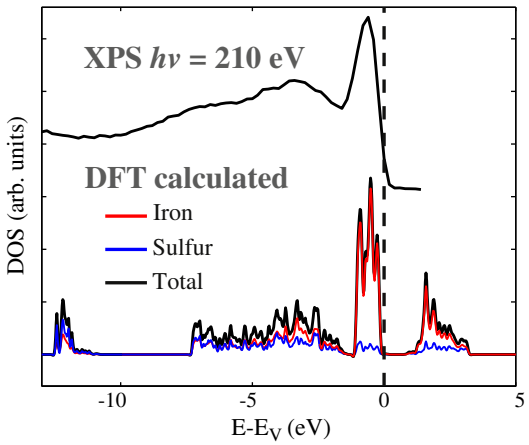


**Fig. 6.** Experimental valence band spectrum obtained using synchrotron X-ray photoelectron spectroscopy (XPS) at photon energy $h\nu = 210$ eV (top) compared against DFT-computed density of states for $FeS_2(100)$ (bottom), also showing partial DOS contributions from iron and sulfur. The dashed line marks the valence band edge.

occupied and effectively screen the electrostatic potential from the tip, reducing the distortion of STS spectra arising from TIBB. By analogy, on metallic materials with freely-available conduction band electrons at the surface, the tip potential drops entirely at the surface and does not extend into the sample. Similarly, extrinsic states (arising from disorder, defects or unintentional contamination), even at low densities of 0.01 monolayers ($3 \times 10^{14}$ cm$^{-2}$) or less, can hold enough charge to significantly affect the magnitude of TIBB and pin $E_F$, e.g. on InN$\left(11\bar{2}0\right)$ [58]. Below, we rationalize these two competing effects in our experimental STS spectra by simulating the effect of different surface state features, the characteristics of which are known from DFT simulations.

### 3.2. Simulated tunneling spectra based on DFT-calculated DOS

We interpret the underlying electronic structure in our measured STS results on $FeS_2$ by simulating the tunneling spectra using an explicit calculation of the electrostatic potential across the tip-vacuum-pyrite system, followed by a full numerical integration of the resulting tunneling current. Using DFT as a guide for the position and distribution of intrinsic and defect-related surface states, we explored several different configurations of surface electronic structure as the input for the tunneling spectra computations and optimized the fit to the experimental STS data in each case. We first compare the DFT-calculated DOS for pyrite with the valence band spectrum of a synthetic sample, measured using synchrotron X-ray photoelectron spectroscopy (Fig. 6). A prominent, Fe 3*d*-related band and the broad, hybridized Fe 3*d* and S 2*p* states between 1 and 7 eV below $E_V$ [59,18] are clearly visible in both the experimental and theoretical data, indicating a general correlation which justifies the use of this DFT data in guiding our analysis.

To investigate the origin of the apparent 0.5 eV surface $E_g$ in the STS results we considered the calculated DOS in energy region surrounding the bulk band gap (approximately $E_V - 0.5$ eV $\leq E \leq E_V + 1.5$ eV) and present here the results for four different simulated electronic structures, which could conceivably give rise to the experimental tunneling spectra. These four models are based on DFT calculations for the bulk crystal (Fig. 7a), a pristine (stoichiometric) surface (Fig. 7d, g), and a defective surface containing both charge neutral $V_{Fe}$ and $V_S$ (Fig. 7j). For the purposes of simulating the tunneling current as a function of bias, each of these characteristic DOS distributions was converted to a simplified representation with inputs for the bulk valence and conduction bands and the requisite surface states. The computed tunneling current that resulted from the different simulated DOS representations was compared to the experimental STS results from Fig. 4.

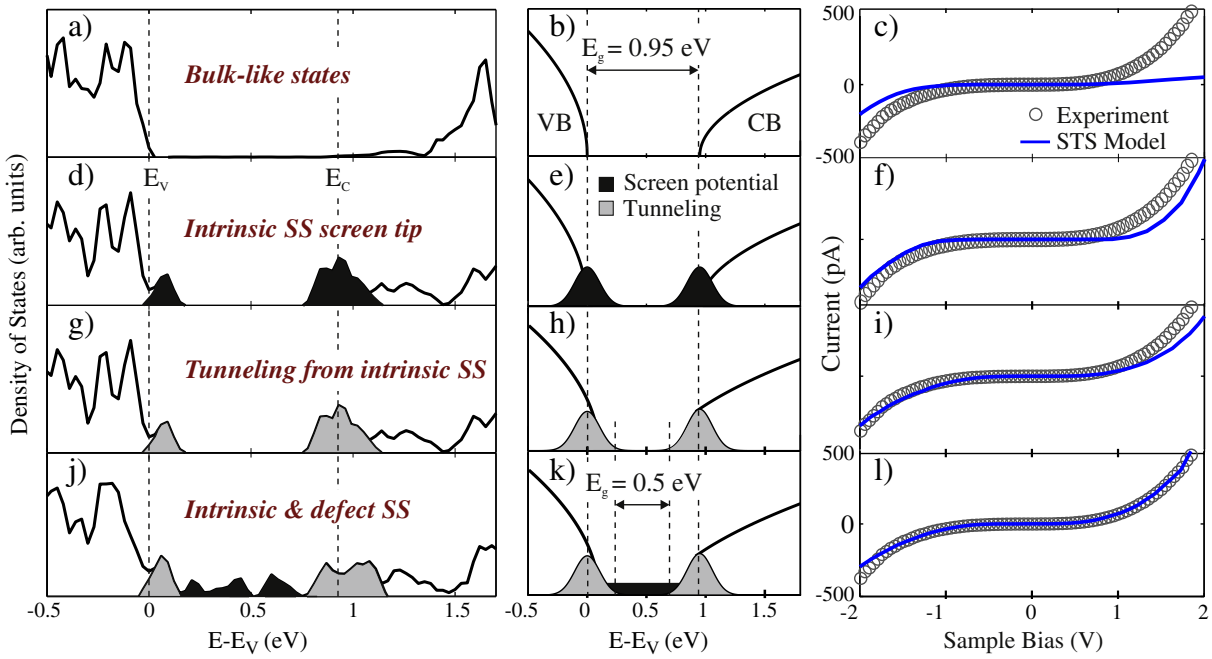


**Fig. 7.** (Left column) density of states (DOS) calculated by density functional theory (DFT) with (middle column) their corresponding, simplified analogs used in tunneling spectroscopy modeling. The shaded regions correspond to surface states (SS's) that either just screen tip potential (black) or, alternatively, contribute to the tunneling current (gray) in the tunneling spectra model input. (Rightmost column) the output from each tunneling spectrum model (solid line) is displayed alongside the same, repeated experimental scanning tunneling spectroscopy (STS) result (open circles), corresponding to a tip-sample separation of so as described in the main text. (a), (b) and (c): bulk-like electronic structure with band gap $E_g = 0.95$ eV and no SS's. (d), (e) and (f) include intrinsic SS's at the $FeS_2(100)$ surface, bordering the band edges but not contributing to tunneling current ($i_{tunn}$) within the fundamental, bulk $E_g$. (g), (h) and (i): the intrinsic SS's now mediate tunneling and the band gap is reduced to 0.5 eV. (j), (k), and (l) correspond to a $FeS_2(100)$ surface with reduced $E_g$ of 0.5 eV containing 12.5% iron point defects ($V_{Fe}$) and sulfur monovacancies ($V_S$).

The four theoretical electronic structures that were matched to the experimental data can be described in more detail as:

1. $FeS_2$ bulk-like density of states as calculated by DFT (Fig. 7a). In the simplified STS model, the VB and CB extrema are separated by an assumed bulk band gap of 0.95 eV and no surface states exist (Fig. 7b).
2. Pristine $FeS_2(100)$ surface density of states, including intrinsic surface states arising from Fe dangling bonds (Fig. 7d). In the theoretical tunneling spectra input (Fig. 7e), a double Gaussian distribution of surface states is included, straddling the VB and CB edges. The density of surface states is set to $6.8 \times 10^{14}$ $cm^{-2}\cdot eV^{-1}$, consistent with the density of Fe dangling bonds at the unreconstructed (100) surface. The charge neutrality level $E_N$ is fixed exactly halfway between the VB maximum and CB minimum, while the FWHM and centroid energies of the surface states were optimized within a reasonable range to provide the closest match to experiment. In this model, the intrinsic surface states can accumulate or deplete in charge depending on the applied bias, and thus serve to screen the tip potential, but do not produce $i_{tunn}$. $E_g$ is still 0.95 eV at the surface.
3. Pristine $FeS_2(100)$ surface density of states, similar to that described in Model (2), but we now postulate that intrinsic surface states are homogeneously connected to the bulk VB and CB. Therefore, surface states are not explicitly defined in this model, but rather the bulk $E_g$ in the input is decreased from 0.95 to 0.5 eV, to approximate the tunneling contribution of intrinsic surface states (Fig. 7h). It is important to note that no surface states were explicitly defined in the computations employing this model so no $E_F$ pinning would be expected. We include the gray, double Gaussian states in Fig. 7h merely to draw the eye to how they effectively reduce the surface $E_g$.
4. Defective $FeS_2(100)$ surface density of states. The surface $E_g$ is reduced to 0.5 eV by the intrinsic surface states, as in Model (3), but we also include defect states from $V_{Fe}$ and $V_S$ with 12.5% surface coverage each, i.e. density of $8.5 \times 10^{13}$ $cm^{-2}\cdot eV^{-1}$ (Fig. 7j). In this theoretical tunneling spectrum model, the defect states form a broad band across the width of the reduced $E_g$ and only contribute free charge to screen the tip potential, without contributing further tunneling current (Fig. 7k).

The results for the four different tunneling spectra simulations are presented adjacent to the corresponding DOS graphs in Fig. 7. Together with each simulated curve we also show the same, repeated experimental STS result obtained using set point tunneling conditions of $V_{set} = 1.5$ V and $i_{set} = 200$ pA, equivalent to the reference tip-sample separation of $s_o$ in Fig. 4. As expected, the first model of bulk-like density of states (Fig. 7c), which excludes any surface states, gives a poor fit to the experimental results. In the absence of available free charge at the surface to pin $E_F$, the semiconductor bands are free to shift with the applied bias, and the CB (VB) edge is dragged to higher (lower) energies with increasing positive (negative) bias. The apparent surface $E_g$ width is therefore >0.95 eV. The second model (Fig. 7f) with surface-localized, non-tunneling intrinsic states approximates the experimental result better, but still does not reliably capture the small size of the zero tunnel current region, nominally corresponding to $E_g$, which is 0.3–0.5 eV larger than the experimental STS results would suggest. A parametric sensitivity study was conducted, and no adjustment of the relative surface state positions or widths produced a fit better than that shown in Fig. 7f, as quantified by minimizing the root mean squared (RMS) difference between the simulated and experimental results (see Supp. Info.). We conclude that the effect of these intrinsic surface states extends beyond a simple screening of the tip potential distribution, as they are defined in the tunneling spectrum model. Consequently, close replication of the experimental spectra can instead be achieved by defining a narrower forbidden energy region $E_g$ in the model input, simulating the case where significant tunneling current originates from the surface states when the bias is swept across biases in the range of approximately $\pm 0.4$ V and below. In Fig. 7i the intrinsic surface states are included continuously with the VB and CB in this manner, i.e., the $E_g$ for the simulation is reduced now to only 0.5 eV. This input produces simulated tunneling currents that match the experiment much better around the zero current region. However, the best fit to the experimental data was achieved when we further include a broad, distributed band of defect states that simulate a 12.5% concentration of both $V_{Fe}$ and $V_S$, at the surface (Fig. 7l). In the model these defect states do not mediate electron tunneling but their effect on the simulated spectrum is to reduce the effect of TIBB by screening the tip potential. Physically, we interpret this to mean that the defect surface states that exist within $E_g$ are too dilute and sparsely distributed to contribute significantly to tunneling and thus further reduce $E_g$. Nevertheless, their presence sufficiently affects the tunneling spectra through $E_F$ pinning. To help understand the lack of measured tunneling current from inter-band defect states, in Fig. 8 we compare the band

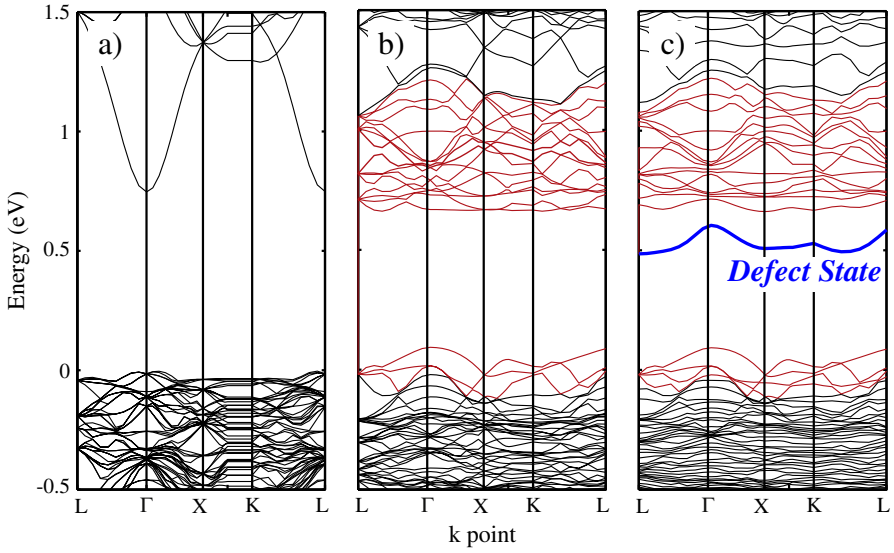


**Fig. 8.** Density functional theory (DFT)-computed band structures for (a) bulk $FeS_2$, (b) a 4-layer surface slab with (100) termination, where we show in the red region the additional bands arising from intrinsic surface states, and (c) the same surface slab but containing a single sulfur vacancy $V_S$ in the topmost layer. The single band coming from the defect is highlighted with a bold, blue line.

structure of bulk $FeS_2$ alongside that of a pristine (100) surface and a defective (100) surface containing a 12.5% concentration of $V_S$, as calculated by DFT. The additional, intrinsic surface state bands – highlighted in red in Fig. 8b, c – form a dense network of states that overlap continuously with the bulk VB and CB. By comparison, the $V_S$ defect state is manifested in a single, isolated band 0.2–0.3 eV below $E_C$. Moreover, we see that the minimum energy point on this defect band clearly dips down at the L point of the Brillouin zone. During the tunneling process, the perpendicular wave vector for the electron $k_\perp$ is relatively small compared to those from intrinsic surface bands, where the empty-state minimum is very flat across the entire $k$ point range shown. Together, these facts suggest that the tunneling from intrinsic surface states would be much stronger than for the defect states, explaining why we observe the intrinsic surface states directly in the experimental tunneling spectra, but the defect states have a more subtle effect.

In order to quantify the width of the surface $E_g$ from the experimental data, a sensitivity analysis of Model (4) was performed with the range $0.3 \leq E_g \leq 0.6$ as the input. The results plotted with logarithmically displayed current in Fig. 9 indicate that a best fit to experimental tunneling current can conceivably be achieved with $E_g = 0.4 \pm 0.1$ eV.

The close match between the experimental and the simulated tunneling spectrum results suggest that the presence of dangling bond surface states on the $FeS_2$(100) free surface leads to a reduction in $E_g$ by ~0.5 eV over the accepted bulk $E_g$ of 0.95 eV. These intrinsic surface states form continuous bands connected to the bulk electronic states and therefore offer available energy levels into which and from which electron tunneling can occur in the presence of the biased probe tip. In contrast, surface states arising from distributed point defects do not contribute to electron tunneling during STS, but instead provide states across a broad range of energies within the fundamental surface $E_g$ that can accrue additional charge from the bulk. This acts to pin the Fermi level and moderate the amount of TIBB during STS. By accounting for both of these surface contributions in tandem, the theoretical model most accurately replicates the experimental STS data. The requirement for such a seemingly high surface defect concentration of 12.5% in the model raises the question of whether this is realistic for a pristine $FeS_2$(100) surface. The existence of a vacant site at one in every eight surface-bound sulfur sites, with a correspondingly similar density of vacant iron sites, would imply one cation and one anion vacancy per four surface unit cells. As we have already discussed, there is a large body of XPS evidence suggesting that up to 20% of pristine pyrite surfaces can comprise $V_S$, even at ambient temperatures of 298 K, including our work in parallel to this study [30]. Likewise, high concentrations of surface $V_{Fe}$ have been imaged on pyrite by STM [32]. It is probable that the synthetic samples used in the current work contain a reasonable concentration of $V_{Fe}$ in addition to the expected $V_S$, given the sulfur-rich conditions of single crystal synthesis. Therefore the assumption of 12.5% as an average for both types of ionic point defect seems plausible. In addition, the effect of extrinsic $(S\text{-}Br)^{2-}$ defects – a known source of impurity in CVT-grown pyrite [9] – has not been considered in our analysis. Although the surface states associated with these defects would be localized at the defects themselves, there is evidence to suggest that vacancies (as well as other defects such as step edges, substitutional dopants and intersecting dislocations) can affect the electronic structure at nanometer distances through the redistribution of surface charge [60–62]. Fig. 10 displays the charge density difference between a supercell of four unit cells of $FeS_2$(100) containing a charge-neutral $V_S$ defect and that of the perfect host, with an isosurface of $\pm 0.014$ e/Å$^3$. The delocalized positive and negative charge resulting from the $V_S$ defect is distributed over almost the entire $2 \times 2$ unit cell area of the simulation, equivalent to approximately $10.8 \times 10.8$ Å$^2$ on the surface. This extent of delocalization would suggest that the charge from a density of only 12.5% $V_S$ on the surface could affect the experimental tunneling spectroscopy measurement, regardless of the exact location that the probe tip is placed during the data acquisition.

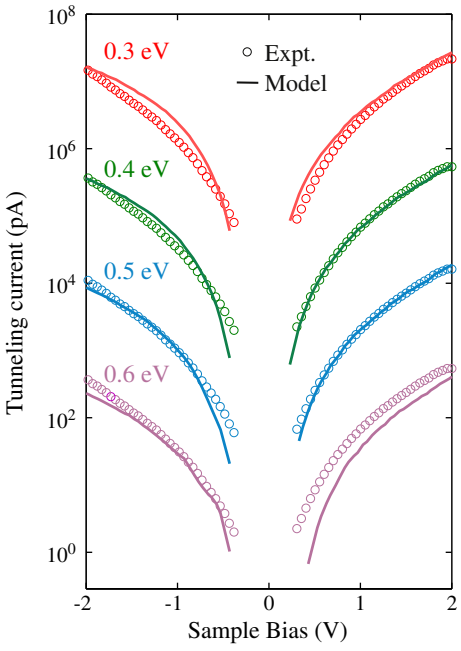


**Fig. 9.** Comparison of experimentally measured tunneling current–voltage $i(V)$ spectrum (open circles, $V_{set} = 1.5$ V and $i_{set} = 200$ pA), with defective $FeS_2$(100) surface Model (4) and four different magnitudes of $E_g$ as listed beside each curve: 0.3, 0.4, 0.5 and 0.6 eV. The absolute values on the tunneling current scale are arbitrary and the curves have been separated by a uniform multiplication of the current data for ease of comparison. We have omitted showing the experimental and modeled data below a current of 1 pA which is the instrument resolution for experimental data acquisition.

## 4. Conclusions

An accurate, quantitative assessment of the surface electronic structure of semiconducting pyrite, $FeS_2$(100), is necessary for understanding the behavior of pyrite in a wide range of applications, including geochemical, bio-catalytic, and corrosion processes, as well as pyrite's

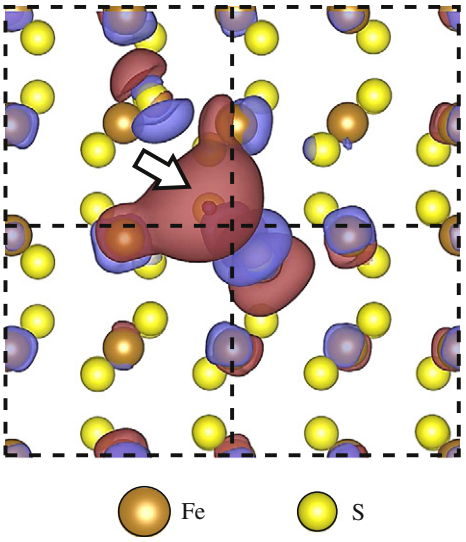


**Fig. 10.** Visualization of $FeS_2$(100) surface charge $q$ surrounding a single sulfur point defect ($V_S$) located at the arrow. We only show the difference in $q$ between the defective and defect-free surfaces, i.e. $\Delta q(V_S - S)$. Positive and negative $\pm 0.014$ e/Å$^3$ isosurfaces are colored in red and blue, respectively. Unit cell edges are shown as dashed lines; one defect in this area corresponds to a $V_S$ concentration of 12.5%.

photovoltaic and photoelectrochemical properties. While scanning tunneling spectroscopy is an ideal tool for this purpose, the analysis is complicated by the well-known effect of tip-induced band bending, the presence of intrinsic surface states, and the additional effects of defect states associated with native ionic vacancies and other defects. We performed systematic STS measurements on synthetic $FeS_2$ single crystals at different tip-sample separations and demonstrated that the apparent surface band gap is consistently $0.4 \pm 0.1$ eV, or ~0.55 eV smaller than the widely-accepted bulk band gap of 0.95 eV for pyrite. By basing our tunneling current simulations on methodically varied, simplified DFT-calculated electronic structures, we link the origin of this reduction in $E_g$ to the presence of intrinsic surface states from Fe dangling bonds at the free surface termination. The electronic bands arising from the intrinsic surface states overlap continuously with the bulk bands. In addition, the experimental tunneling spectra results can be modeled most accurately if a second distribution of surface states arising from cation and anion vacancies is incorporated into the tunneling current simulations. These defect states do not contribute significantly to overall tunneling current but have an influence on the tunneling spectra by accumulating charge at the pyrite surface, which screens the tip potential during measurement and pins the Fermi level. Our findings confirm the influence of both intrinsic and defect surface states on the electronic structure of pyrite. The presence of a reduced band gap on the surface, as well as the existence of defect states within the band gap, hold implications for electronic processes such as charge transfer during electrochemical redox reactions.

Supplementary data to this article can be found online at http://dx.doi.org/10.1016/j.susc.2013.08.014.

## Acknowledgments

We gratefully acknowledge the support provided by BP Plc. through the BP-MIT Center for Materials and Corrosion Research. We thank R.M. Feenstra for the use of his SEMITIP program for performing tunneling current simulations. We are also grateful to D. Mullins and P. Albrecht for the use of the U12a beamline for XPS measurements. The U12a beamline is supported by the Division of Chemical Sciences, Geosciences, and Biosciences, Office of Basic Energy Sciences, U.S. Department of Energy, under contract DE-AC05-00OR22725 with Oak Ridge National Laboratory, managed and operated by UT-Battelle, LLC. Use of the National Synchrotron Light Source, Brookhaven National Laboratory, was supported by the U.S. Department of Energy, Office of Science, Office of Basic Energy Sciences, under Contract No. DE-AC02-98CH10886.

## References

[1] J.M. Guevremont, J. Bebie, A.R. Elsetinow, D.R. Strongin, M.A.A. Schoonen, Environ. Sci. Technol. 32 (23) (1998) 3743.
[2] R. Murphy, D.R. Strongin, Surf. Sci. Rep. 64 (1) (2009) 1.
[3] I. Uhlig, R. Szargan, H.W. Nesbitt, K. Laajalehto, Appl. Surf. Sci. 179 (1–4) (2001) 222.
[4] K.M. Rosso, Mol. Model. Theory Appl. Geosci. 42 (2001) 199.
[5] J. Bebie, M.A.A. Schoonen, Geochem. Trans. 1 (1) (2000) 47.
[6] C. Boehme, D. Marx, J. Am. Chem. Soc. 125 (44) (2003) 13362.
[7] N.N. Nair, E. Schreiner, D. Marx, J. Am. Chem. Soc. 128 (42) (2006) 13815.
[8] M. Caban-Acevedo, M.S. Faber, Y.Z. Tan, R.J. Hamers, S. Jin, Nano Lett. 12 (4) (2012) 1977.
[9] J. Hu, Y.N. Zhang, M. Law, R.Q. Wu, Phys. Rev. B 85 (8) (2012).
[10] R.S. Sun, M.K.Y. Chan, G. Ceder, Phys. Rev. B 83 (23) (2011).
[11] R.S. Sun, M.K.Y. Chan, S.Y. Kang, G. Ceder, Phys. Rev. B 84 (3) (2011).
[12] A. Ennaoui, S. Fiechter, C. Pettenkofer, N. Alonsovante, K. Buker, M. Bronold, C. Hopfner, H. Tributsch, Sol. Energy Mater. Sol. Cells 29 (4) (1993) 289.
[13] J.D. Burton, E.Y. Tsymbal, Phys. Rev. Lett. 107 (16) (2011).
[14] H. Vedage, T.A. Ramanarayanan, J.D. Mumford, S.N. Smith, Corrosion 49 (2) (1993) 114.
[15] V. Heine, Phys. Rev. 138 (6A) (1965) 1689–1696.
[16] L. Kronik, Y. Shapira, Surf. Interface Anal. 31 (10) (2001) 954.
[17] A. Krishnamoorthy, F.W. Herbert, S. Yip, K.J. Van Vliet, B. Yildiz, J. Phys. Condens. Matter 25 (4) (2012) 045004.
[18] M. Bronold, Y. Tomm, W. Jaegermann, Surf. Sci. 314 (3) (1994) L931.
[19] Y. Bi, Y.B. Yuan, C.L. Exstrom, S.A. Darveau, J.S. Huang, Nano Lett. 11 (11) (2011) 4953.
[20] T.R. Yang, J.T. Yu, J.K. Huang, S.H. Chen, M.Y. Tsay, Y.S. Huang, J. Appl. Phys. 77 (4) (1995) 1710.
[21] C.H. Ho, Y.S. Huang, K.K. Tiong, J. Alloys Compd. 422 (2006) 321.
[22] M.Y. Tsay, Y.S. Huang, Y.F. Chen, J. Appl. Phys. 74 (4) (1993) 2786.
[23] C. Wadia, Y. Wu, S. Gul, S.K. Volkman, J.H. Guo, A.P. Alivisatos, Chem. Mater. 21 (13) (2009) 2568.
[24] L.P. Yu, S. Lany, R. Kykyneshi, V. Jieratum, R. Ravichandran, B. Pelatt, E. Altschul, H.A.S. Platt, J.F. Wager, D.A. Keszler, A. Zunger, Adv. Energy Mater. 1 (5) (2011) 748.
[25] H.W. Nesbitt, G.M. Bancroft, A.R. Pratt, M.J. Scaini, Am. Mineral. 83 (9–10) (1998) 1067.
[26] A.G. Schaufuss, H.W. Nesbitt, I. Kartio, K. Laajalehto, G.M. Bancroft, R. Szargan, Surf. Sci. 411 (3) (1998) 321.
[27] J.A. Leiro, S.S. Mattila, K. Laajalehto, Surf. Sci. 547 (1–2) (2003) 157.
[28] S. Mattila, J.A. Leiro, K. Laajalehto, Appl. Surf. Sci. 212 (2003) 97.
[29] K. Andersson, M. Nyberg, H. Ogasawara, D. Nordlund, T. Kendelewicz, C.S. Doyle, G.E. Brown, L.G.M. Pettersson, A. Nilsson, Phys. Rev. B 70 (19) (2004).
[30] F.W. Herbert, K Krishnamoorthy, W. Ma, K.J. Van Vliet, and B. Yildiz. (in preparation), 2013.
[31] Y.N. Zhang, J. Hu, M. Law, R.Q. Wu, Phys. Rev. B 85 (8) (2012).
[32] K.M. Rosso, U. Becker, M.F. Hochella, Am. Mineral. 85 (10) (2000) 1428.
[33] C. Steinhagen, T.B. Harvey, C.J. Stolle, J. Harris, B.A. Korgel, J. Phys. Chem. Lett. 3 (17) (2012) 2352.
[34] K.M. Rosso, U. Becker, M.F. Hochella, Am. Mineral. 84 (10) (1999) 1535.
[35] C.M. Eggleston, J.J. Ehrhardt, W. Stumm, Am. Mineral. 81 (9–10) (1996) 1036.
[36] F.R. Fan, A.J. Bard, J. Phys. Chem. 95 (5) (1991) 1969.
[37] D. Siebert, W. Stocker, Phys. Status Solidi A Appl. Res. 134 (1) (1992) K17.
[38] J.A. Stroscio, R.M. Feenstra, A.P. Fein, Phys. Rev. Lett. 57 (20) (1986) 2579.
[39] R.M. Feenstra, Phys. Rev. B 50 (7) (1994) 4561.
[40] R.M. Feenstra, Y. Dong, M.P. Semtsiv, W.T. Masselink, Nanotechnology 18 (4) (2007).
[41] N. Ishida, K. Sueoka, R.M. Feenstra, Phys. Rev. B 80 (7) (2009).
[42] G. Willeke, O. Blenk, C. Kloc, E. Bucher, J. Alloys Compd. 178 (1992) 181.
[43] U. Becker, A.W. Munz, A.R. Lennie, G. Thornton, D.J. Vaughan, Surf. Sci. 389 (1–3) (1997) 66.
[44] S. Chaturvedi, R. Katz, J. Guevremont, M.A.A. Schoonen, D.R. Strongin, Am. Mineral. 81 (1–2) (1996) 261.
[45] S.L. Dudarev, G.A. Botton, S.Y. Savrasov, C.J. Humphreys, A.P. Sutton, Phys. Rev. B 57 (3) (1998) 1505.
[46] K. Momma, F. Izumi, J. Appl. Crystallogr. 41 (2008) 653.
[47] R.M. Feenstra, www.andrew.cmu.edu/user/feenstra/semitip-v62011.
[48] R.M. Feenstra, J. Vac. Sci. Technol. B Microelectron. Nanometer Struct. 21 (5) (2003) 2080.
[49] Y. Dong, R.M. Feenstra, M.P. Semtsiv, W.T. Masselink, J. Appl. Phys. 103 (7) (2008).
[50] S. Gaan, G.W. He, R.M. Feenstra, J. Walker, E. Towe, J. Appl. Phys. 108 (11) (2010).
[51] C.K. Egan, A. Choubey, A.W. Brinkman, Surf. Sci. 604 (19–20) (2010) 1825.
[52] J. Tersoff, D.R. Hamann, Phys. Rev. B 31 (2) (1985) 805.
[53] L. Ivanova, S. Borisova, H. Eisele, M. Dahne, A. Laubsch, P. Ebert, Appl. Phys. Lett. 93 (19) (2008).
[54] R.M. Feenstra, Phys. Rev. B 44 (24) (1991) 13791.
[55] R. Maboudian, K. Pond, V. Bresslerhill, M. Wassermeier, P.M. Petroff, G.A.D. Briggs, W.H. Weinberg, Surf. Sci. 275 (1–2) (1992) L662.
[56] A. Sabitova, Ph. Ebert, A. Lenz, S. Schaafhausen, L. Ivanova, M. Dahne, A. Hoffmann, R.E. Dunin-Borkowski, A. Forster, B. Grandidier, H. Eisele, Appl. Phys. Lett. 102 (2) (2013) 021608-4.
[57] Ph. Ebert, L. Ivanova, H. Eisele, Phys. Rev. B 80 (8) (2009) 085316.
[58] P. Ebert, S. Schaafhausen, A. Lenz, A. Sabitova, L. Ivanova, M. Dahne, Y.L. Hong, S. Gwo, H. Eisele, Appl. Phys. Lett. 98 (6) (2011).
[59] G.L. Zhao, J. Callaway, M. Hayashibara, Phys. Rev. B 48 (21) (1993) 15781.
[60] Ph. Ebert, M. Heinrich, M. Simon, K. Urban, M.G. Lagally, Phys. Rev. B 51 (15) (1995) 9696.
[61] Ph. Ebert, Surf. Sci. Rep. 33 (1999) 121.
[62] U. Becker, K.M. Rosso, Am. Mineral. 86 (7–8) (2001) 862.